INTERNODES: an accurate interpolation-based method for coupling the Galerkin solutions of PDEs on subdomains featuring non-conforming interfaces

Deparis, S.; Forti, D.; Gervasio, P.; Quarteroni, A.

INTERNODES: an accurate interpolation-based method for coupling the Galerkin solutions of PDEs on subdomains featuring non-conforming interfaces

Simone Deparis[a], Davide Forti[a,*], Paola Gervasio[b], Alfio Quarteroni[a,c]

[a]*CMCS-MATHICSE, École Polytechnique Fédérale de Lausanne, Station 8, CH-1015 Lausanne, Switzerland*
[b]*DICATAM, Università degli Studi di Brescia, via Branze 38, I-25123 Brescia, Italy*
[c]*MOX, Politecnico di Milano, via Bonardi 9, Milano, 20133, Italy (on leave)*

Abstract

We are interested in the approximation of partial differential equations on domains decomposed into two (or several) subdomains featuring non-conforming interfaces. The non-conformity may be due to different meshes and/or different polynomial degrees used from the two sides, or even to a geometrical mismatch. Across each interface, one subdomain is identified as master and the other as slave. We consider Galerkin methods for the discretization (such as finite element or spectral element methods) that make use of two interpolants for transferring information across the interface: one from master to slave and another one from slave to master. The former is used to ensure continuity of the primal variable (the problem solution), while the latter for the dual variable (the normal flux). In particular, since the dual variable is expressed in weak form, we first compute a strong representation of the dual variable from the slave side, interpolate it, transform the interpolated quantity back into weak form and assign it to the master side. In case of slightly non-matching geometries, we use a radial-basis function interpolant instead of Lagrange interpolant.

We name the proposed method INTERNODES (INTERpolation for NOnconforming DEcompositionS). It can be regarded as an alternative to the mortar element method and it is much simpler to implement in a numerical code. We show on two dimensional problems that by using the Lagrange interpolation we obtain at least as good convergence results as with the mortar element method with any order of polynomials. When using low or-

---
[*]Corresponding author. E-mail: davide.forti@epfl.ch, Phone:+41 21 6930352, Fax:+41 21 6935510.

der polynomials, the radial-basis interpolant leads to the same convergence properties as the Lagrange interpolant. We conclude with a comparison between INTERNODES and a standard conforming approximation in a three dimensional case.

1. Introduction

In this paper we propose a new approach for numerically solving elliptic partial differential equations by Galerkin methods on computational domains that are split into two (or several) subdomains featuring "non-conforming interfaces". By this we mean that either a priori independent grids and/or local polynomial degrees are used to discretize each subdomain. More in particular, we refer to these two cases as "grid non-conformity" and "polynomial non-conformity", respectively. A third possible case of non-conforming interfaces that our approach can cover is that of subdomains that face each other through two interfaces that geometrically do not fully agree one another, meaning that the two subdomains may either slightly overlap and/or featuring tiny holes between them (see Figure 3). We name this latter situation of geometrical mismatch as "geometric non- conformity". It may arise when using CAD to generate the two subdomains, e.g. in fluid structure interaction problems in hydrodynamics or aerodynamics [14, 15], or else when generating the computational geometries of lumen and vessel walls from DYCOM images for arterial blood flow dynamics [9, 19].

In all these cases of non-conforming interfaces, a very crucial issue is the way the subdomain solutions communicate across common interfaces. More specifically, at which extent the subdomain solutions and their normal fluxes do match. Our approach proceeds as follows. Across each interface, the subdomain from one side is identified as the master while that from the opposite side as the slave. *We then introduce two different interpolants for transferring information across the interface*: one from master to slave and another one from slave to master. The former is used to ensure continuity of the primal variable (the problem solution), while the latter for ensuring the continuity of the dual variable (the normal flux). In particular, since in each subdomain we are using a Galerkin projection method, the dual variable in the slave domain is available in weak form, *we first compute a strong representation of the dual variable from the slave side, interpolate*

it, transform the interpolated quantity back into weak form and assign the function so obtained to the master side. This is a very distinguishing feature of our method, that we named INTERNODES. Interpolants can be either Lagrangian or built on Radial Basis Functions (RBF). In particular, in case of geometric non-conformity with slightly non-matching geometries, we use RBF interpolants because of their flexibility.

INTERNODES can be regarded as an alternative to the mortar element method, formerly introduced by [3, 4] (see also [2, 16, 22]). It shares similar properties of accuracy and is much simpler to implement in a numerical code. We show on two dimensional problems that using the Lagrange interpolation, INTERNODES attains at least as good convergence results as the mortar element method, for any order of polynomials. When using low order polynomials, the radial-basis functions interpolant leads to the same convergence properties as the Lagrange interpolant. On the other side, our method (being based on interpolation rather than on L^2 projection at interfaces) is far more simple to implement than the mortar method.

The paper is organized as follows. After setting up our elliptic boundary value problem in Section 2, we introduce in Section 3 its Galerkin discretization based on the Finite Element Method (FEM) or the Spectral Element Method (SEM) using non-conforming interfaces. In Section 4 we introduce our slave-to-master and master-to-slave interface intergrid operators (either Lagrangian or RBF based). In Section 5 we formulate our numerical method that makes use of the two intergrid operators: we first formulate it in algebraic terms, then we provide a variational interpretation as a non conforming generalized Galerkin approximation to the original elliptic boudary value problem. In the same Section we show that the mortar method can be recast in the general form of our method and therefore regarded as a special case of it. Section 6 is devoted to an analysis of the numerical results that we obtain for FEM-FEM, FEM-SEM and SEM-SEM couplings when approximating the Dirichlet problem in a 2D domain. The same problem is addressed in Section 7 for the case of geometric non-conformity. More realistic applications are addressed in Sections 8 and 9 where we consider very severe non-conformity for the simulation of near field and far field solutions of diffusion processes around a chimney in two dimensions and a fluid flow past a three dimensional cylinder, respectively. Finally, conclusions are drawn in Section 10.

2. Problem setting

Let $\Omega \subset \mathbb{R}^d$, with $d = 2,\ 3$, be an open domain with Lipschitz boundary $\partial\Omega$. $\partial\Omega_N$ and $\partial\Omega_D$ are suitable disjoint subsets of $\partial\Omega$ such that $\overline{\partial\Omega_D} \cup \overline{\partial\Omega_N} = \partial\Omega$. Given suitable functions f, μ, and α defined on Ω, and g defined on $\partial\Omega_N$, we look for the solution u of the second order elliptic self-adjoint equation

$$
\begin{cases}
Lu \equiv -\nabla \cdot (\mu \nabla u) + \alpha u = f & \text{in } \Omega, \\
u = 0 & \text{on } \partial\Omega_D, \\
\mu \dfrac{\partial u}{\partial n} = g & \text{on } \partial\Omega_N,
\end{cases}
\tag{1}
$$

being n the outward unit normal vector to $\partial\Omega^1$.

If $f \in L^2(\Omega)$, $g \in H^{-1/2}(\partial\Omega_N)$, $\mu, \alpha \in L^\infty(\Omega)$ such that $\exists \mu_0 > 0$, $\mu \geq \mu_0$ and $\alpha \geq 0$, and by setting $V = H^1_{\partial\Omega_D}(\Omega) = \{v \in H^1(\Omega) : \ v|_{\partial\Omega_D} = 0\}$, the weak form of problem (1) reads

$$
\text{find } u \in V : \quad a(u,v) = (f,v)_\Omega \qquad \forall v \in V,
\tag{2}
$$

where

$$
a(u,v) = \int_\Omega (\mu \nabla u \cdot \nabla v + \alpha u v) d\Omega,
\tag{3}
$$

while $(\cdot, \cdot)_\Omega$ denotes the inner product in $L^2(\Omega)$.

For the sake of exposition we partition Ω into two non-overlapping subdomains Ω_1 and Ω_2 such that $\overline{\Omega} = \overline{\Omega_1 \cup \Omega_2}$; we call one *master* (say Ω_1) and the other *slave* (say Ω_2).

Two possible instances of subdomain partitions are shown in Figure 1, where we set $\Gamma = \overline{\Omega}_1 \cap \overline{\Omega}_2$.

3. Discretization

A-priori independent discretizations of either finite element type (FEM) or spectral element type (SEM) are designed in Ω_1 and Ω_2 [5, 17]. SEM will be equivalently named $hp-$FEM (see [21]).

We denote by $\mathcal{T}_{h,k}$ (for $k = 1, 2$) the meshes induced by the discretization in Ω_k and we assume that they satisfy standard regularity requirements (see [17]).

---

[1] The more general situation with non-homogeneous Dirichlet conditions can be formulated as in (1) by using a suitable lifting operator of the Dirichlet datum (see, e.g., [17]).
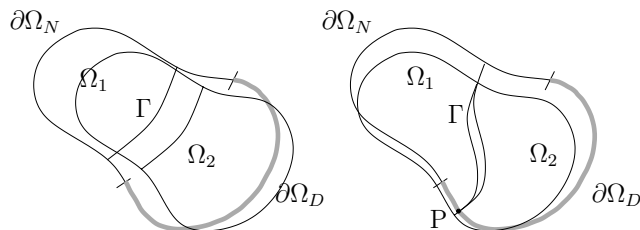
Figure 1: Two possible instances of subdomains partitions in the case $d = 2$. The gray thick curve denotes the Dirichlet boundary $\partial\Omega_D$.
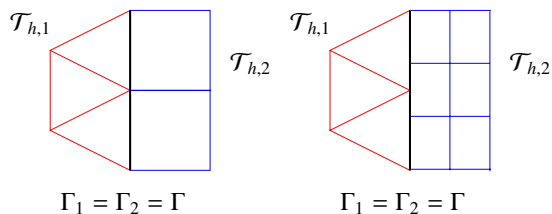

Figure 2: Conforming (at left) and non-conforming (at right) grids at the interface when $d = 2$.

On the interface Γ, we allow the meshes $\mathcal{T}_{h,1}$ and $\mathcal{T}_{h,2}$ to induce either *conforming grids* (see Figure 2, left) or *non-conforming grids* (see Figure 2, right).

In some situations, while discretizing Γ, we could even end up with two non-matching interfaces $\Gamma_1 \neq \Gamma_2$. We refer to this last situation as *non-matching interfaces* or *geometrically non-conforming partitions*. A possible instance is when Γ is a curved line that is discretized by piecewise straight segments, see Figure 3. Another instance may occur when using isogeometric analysis (see [6]).

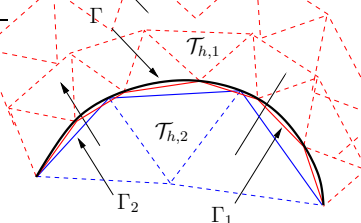In order to unify our theory for both the cases of matching and non-

Figure 3: A situation with non-matching interfaces Γ_1 and Γ_2 in the case $d = 2$.

matching interfaces, from now on we will refer to Γ_1 and Γ_2 separately, understanding that $\Gamma_1 = \Gamma_2 = \Gamma$ in the geometrically conforming case.

In both Ω_k ($k = 1, 2$) we introduce the finite elements approximation spaces

$$X_{h_k}^{p_k} = \{v \in C^0(\overline{\Omega}_k) \, : \, v_{|T} \in Q_p, \ \forall T \in \mathcal{T}_{h,k}\}, \tag{4}$$

where $Q_p = \mathbb{P}_p$ in the simplicial case and $Q_p = \mathbb{Q}_p \circ \mathbf{F}_T^{-1}$ for quads, being $\mathbf{F}_T$ the C^1 diffeomorphism that maps the reference element $\hat{T}$ into T ([17]).

Another situation we would like to address is that when different polynomial degrees are used on the two subdomains (*polynomial non-conformity*). Finally, we would also like to address the case in which one couples FEM on simplicials from one side with SEM on quads from the other side, with different polynomial degrees.

Generally speaking, we call *non-conforming* a situation where one (or several) of the previous cases (non-conforming grids, non-matching interfaces, polynomial non-conformity) arises.

For $k = 1, 2$, we introduce the finite dimensional subspaces $V_{k,\delta}$ of $V_k = H_{\partial\Omega_D \cap \partial\Omega_k}^1(\Omega_k)$, where δ stands for discretization, more precisely

$$V_{k,\delta} = X_{h_k}^{p_k} \cap V_k. \tag{5}$$

We identify the Lagrange basis of $V_{k,\delta}$ as $\{\Phi_i^{(k)}\}_i$, for $k = 1, 2$. Then, we define the subspaces of V

$$\mathring{V}_{k,\delta} = \{v \in V : v|_{\Omega_k} \in V_{k,\delta} \text{ and } v|_{\Omega \setminus \Omega_k} = 0\}, \quad N_k = \dim(\mathring{V}_{k,\delta}). \tag{6}$$

Notice that the restriction on Γ of any $v \in \mathring{V}_{k,\delta}$ is null.

4. Intergrid operators

Let us introduce the discrete trace functional spaces

$$\Lambda_{k,\delta} = \{\varphi = v|_{\Gamma_k}, \ v \in V_{k,\delta}\}, \quad n_k = \dim(\Lambda_{k,\delta}), \tag{7}$$

and identify a basis of $\Lambda_{k,\delta}$ as $\{\lambda_j^{(k)}\}_{j=1}^{n_k}$. We introduce two linear operators

$$\Pi_{12} : \Lambda_{2,\delta} \to \Lambda_{1,\delta}, \qquad \Pi_{21} : \Lambda_{1,\delta} \to \Lambda_{2,\delta} \tag{8}$$

that realize the *intergrid transfer*. We consider two different instances:

1. Lagrange interpolation,
2. Radial Basis Function (RBF) interpolation, in particular RL-RBF [7].

For reader's convenience, we define here the interpolation operators. For $k = 1, 2$ and $i = 1, \ldots, n_k$, let $\mathbf{x}_i^{(\Gamma_k)} \in \Gamma_k$ denote the degrees of freedom associated with the Lagrange basis functions $\lambda_i^{(k)}$.

The Lagrange interpolation operator Π_{21} is characterized as follows. Let us consider a function $\eta_{1,\delta} \in \Lambda_{1,\delta}$, then $\Pi_{21}\eta_{1,\delta}$ can be written w.r.t. the basis $\{\lambda_i^{(2)}\}$ of $\Lambda_{2,\delta}$ as

$$(\Pi_{21}\eta_{1,\delta})(\mathbf{x}) = \sum_{i=1}^{n_2} (\Pi_{21}\eta_{1,\delta})(\mathbf{x}_i^{(\Gamma_2)})\lambda_i^{(2)}(\mathbf{x}), \quad \forall \mathbf{x} \in \Gamma_2. \tag{9}$$

By expanding $\eta_{1,\delta}$ with respect to the basis functions $\lambda_j^{(1)}$ of $\Lambda_{1,\delta}$ we have

$$\eta_{1,\delta}(\mathbf{x}) = \sum_{j=1}^{n_1} \eta_{1,\delta}(\mathbf{x}_j^{(\Gamma_1)})\lambda_j^{(1)}(\mathbf{x}) \qquad \forall \mathbf{x} \in \Gamma_1,$$

and then, for any $\mathbf{x} \in \Gamma_2$,

$$(\Pi_{21}\eta_{1,\delta})(\mathbf{x}) = \sum_{i=1}^{n_2} \left(\sum_{j=1}^{n_1} \eta_{1,\delta}(\mathbf{x}_j^{(\Gamma_1)})(\Pi_{21}\lambda_j^{(1)})(\mathbf{x}_i^{(\Gamma_2)}) \right) \lambda_i^{(2)}(\mathbf{x}).$$

Finally, denoting by $\boldsymbol{\eta}_1$ the array in $\mathbb{R}^{n_1}$ whose components are the nodal values $\eta_{1,\delta}(\mathbf{x}_i^{(\Gamma_1)})$, for $i = 1, \ldots, n_1$, and by

$$(R_{21})_{ij} = (\Pi_{21}\lambda_j^{(1)})(\mathbf{x}_i^{(\Gamma_2)}), \quad i = 1, \ldots, n_2, \ j = 1, \ldots, n_1, \tag{10}$$

the entries of the matrix associated with the operator Π_{21}, we can write

$$(\Pi_{21}\eta_{1,\delta})(\mathbf{x}_i^{(\Gamma_2)}) = (R_{21}\boldsymbol{\eta}_1)_i, \quad i = 1, \ldots, n_2.$$

By proceeding in a similar way for Π_{12}, we denote the entries of the matrix associated with the operator Π_{12} by

$$(R_{12})_{ij} = (\Pi_{12}\lambda_j^{(2)})(\mathbf{x}_i^{(\Gamma_1)}), \quad i = 1, \ldots, n_1, \ j = 1, \ldots, n_2, \tag{11}$$

so that

$$(\Pi_{12}\eta_{2,\delta})(\mathbf{x}_i^{(\Gamma_1)}) = (R_{12}\boldsymbol{\eta}_{2,\delta})_i, \quad i = 1, \ldots, n_1.$$

The RL-RBF interpolation operators are defined as in [7] and they read

$$(\Pi_{21}\eta_{1,\delta})(\mathbf{x}) = \frac{\sum_{i=1}^{n_1} \gamma_i^{\eta_{1,\delta}}\phi(\|\mathbf{x} - \mathbf{x}_i^{(\Gamma_1)}\|, r_i)}{\sum_{i=1}^{n_1} \gamma_i^1\phi(\|\mathbf{x} - \mathbf{x}_i^{(\Gamma_1)}\|, r_i)}, \tag{12}$$

$$(\Pi_{12}\eta_{2,\delta})(\mathbf{x}) = \frac{\sum_{i=1}^{n_2} \gamma_i^{\eta_{2,\delta}}\phi(\|\mathbf{x} - \mathbf{x}_i^{(\Gamma_2)}\|, r_i)}{\sum_{i=1}^{n_2} \gamma_i^1\phi(\|\mathbf{x} - \mathbf{x}_i^{(\Gamma_2)}\|, r_i)}, \tag{13}$$

where ϕ is the locally supported radial basis function, $r_i \in \mathbb{R}$ is the local support of the basis function, and γ_i^f are the weights of the interpolant of the function f ($f \equiv 1$ denotes the constant function $f(x) = 1$) and they are determined by imposing the interpolation constraints at either the nodes $\mathbf{x}_i^{(\Gamma_2)}$ ($i = 1, \ldots, n_2$) for Π_{21}, or at $\mathbf{x}_i^{(\Gamma_1)}$ ($i = 1, \ldots, n_1$) for Π_{12}.

Then, we define two linear and continuous extension operators $E_k : \Lambda_{k,\delta} \to V_{k,\delta}$, for $k = 1, 2$. The simplest choice is to use the interpolation operator that extends $\lambda_j^{(k)} \in \Lambda_{k,\delta}$ by setting to zero its values at all nodes of $\overline{\Omega}_k$ not belonging to Γ_k.

The *interface* space is defined as

$$V_{\Gamma_1} = \{\varphi \in L^2(\Omega) : \exists \lambda_1 \in \Lambda_{1,\delta} : \quad \begin{aligned} \varphi|_{\Omega_1} &= E_1\lambda_1, \\ \varphi|_{\Omega_2} &= E_2(\Pi_{21}\lambda_1)\}. \end{aligned} \tag{14}$$

Note that its elements are functions defined in the whole $\overline{\Omega}$. We denote a basis of V_{Γ_1} as $\{\lambda_j^e\}_{j=1}^{n_1}$, where "$e$" stands for "extension". There is a one-to-one map between $\lambda_j^{(1)}$ (the jth basis function of $\Lambda_{1,\delta}$) and λ_j^e, and λ_j^e satisfies $\lambda_j^e|_{\Omega_1} = E_1\lambda_j^{(1)}$ and $\lambda_j^e|_{\Omega_2} = E_2(\Pi_{21}\lambda_j^{(1)})$.

Then we set

$$V_\delta = \mathring{V}_{1,\delta} \oplus \mathring{V}_{2,\delta} \oplus V_{\Gamma_1}. \tag{15}$$

Notice that $V_\delta \not\subset V$ in general.

5. Non-conforming formulation

For $k = 1, 2$, we define the bilinear forms

$$a_k : V_k \times V_k \to \mathbb{R} : \quad a_k(u, v) = \int_{\Omega_k} (\mu \nabla u \cdot \nabla v + \alpha uv) d\Omega, \tag{16}$$

the matrices

$$\begin{aligned}
(A_{kk})_{ij} &= a_k(\Phi_j^{(k)}, \Phi_i^{(k)}), & i, j &= 1, \ldots, N_k, \\
(A_{k,\Gamma_k})_{ij} &= a_k(E_k\lambda_j^{(k)}, \Phi_i^{(k)}), & i &= 1, \ldots, N_k, \\
& & j &= 1, \ldots, n_k, \\
(A_{\Gamma_k,k})_{ij} &= a_k(\Phi_j^{(k)}, E_k\lambda_i^{(k)}), & i &= 1, \ldots, n_k, \\
& & j &= 1, \ldots, N_k, \\
(A_{\Gamma_k,\Gamma_k})_{ij} &= a_k(E_k\lambda_j^{(k)}, E_k\lambda_i^{(k)}), & i, j &= 1, \ldots, n_k.
\end{aligned} \tag{17}$$

(note that $(A_{\Gamma_1,1})_{ij} = a_1(\Phi_j^{(1)}, \lambda_i^e)$) and the vectors

$$
\begin{aligned}
\mathbf{f}_k &= (f, \Phi_i^{(k)})_{\Omega_k}, & i = 1, \ldots, N_k, \\
\mathbf{f}_{\Gamma_k} &= (f, E_k \lambda_i^{(k)})_{\Omega_k}, & i = 1, \ldots, n_k.
\end{aligned}
\tag{18}
$$

In the special case of fully conforming discretizations (that is both grid and polynomial conformity, with $\Gamma_1 = \Gamma_2 = \Gamma$ and $n_1 = n_2$), the well-known algebraic domain decomposition form of the weak original problem (2) reads ([18])

$$
\begin{bmatrix}
A_{1,1} & 0 & A_{1,\Gamma_1} \\
0 & A_{2,2} & A_{2,\Gamma_2} \\
A_{\Gamma_1,1} & A_{\Gamma_2,2} & A_{\Gamma_1,\Gamma_1} + A_{\Gamma_2,\Gamma_2}
\end{bmatrix}
\begin{bmatrix}
\mathbf{u}_1 \\
\mathbf{u}_2 \\
\mathbf{u}_\Gamma
\end{bmatrix}
=
\begin{bmatrix}
\mathbf{f}_1 \\
\mathbf{f}_2 \\
\mathbf{f}_{\Gamma_1} + \mathbf{f}_{\Gamma_2}
\end{bmatrix},
\tag{19}
$$

where $\mathbf{u}_k \in \mathbb{R}^{N_k}$ is the array of the nodal values of $u_{k,\delta} = u_\delta|_{\overline{\Omega}_k \backslash \Gamma_k}$, for $k = 1, 2$, while $\mathbf{u}_\Gamma \in \mathbb{R}^{n_1}$ is the array of the nodal values of $u_\delta|_\Gamma$, and $u_\delta \in V_\delta \subset V$ is the solution of the conforming Galerkin problem $a(u_\delta, v_\delta) = (f, v_\delta)_\Omega$ for any $v_\delta \in V_\delta$.

In the non-conforming case we need further matrices: $M_{\Gamma_k} \in \mathbb{R}^{n_k}$, that is the mass matrix associated with the interface Γ_k, and the matrices $R_{12} \in \mathbb{R}^{n_1 \times n_2}$ and $R_{21} \in \mathbb{R}^{n_2 \times n_1}$ defined in (10) and (11), respectively.

Finally, by setting

$$
Q_{21} = R_{21}, \qquad Q_{12} = M_{\Gamma_1} R_{12} M_{\Gamma_2}^{-1},
\tag{20}
$$

the *non-conforming* generalization of (19) reads

$$
\begin{bmatrix}
A_{1,1} & 0 & A_{1,\Gamma_1} \\
0 & A_{2,2} & A_{2,\Gamma_2} Q_{21} \\
A_{\Gamma_1,1} & Q_{12} A_{\Gamma_2,2} & A_{\Gamma_1,\Gamma_1} + Q_{12} A_{\Gamma_2,\Gamma_2} Q_{21}
\end{bmatrix}
\begin{bmatrix}
\mathbf{u}_1 \\
\mathbf{u}_2 \\
\mathbf{u}_{\Gamma_1}
\end{bmatrix}
$$
$$
=
\begin{bmatrix}
\mathbf{f}_1 \\
\mathbf{f}_2 \\
\mathbf{f}_{\Gamma_1} + Q_{12} \mathbf{f}_{\Gamma_2}.
\end{bmatrix}.
\tag{21}
$$

Notice that, in the fully conforming case, Q_{12} and Q_{21} coincide with the identity matrix of size $n_1 = n_2$ (and (21) returns (19)).

5.1. Variational formulation

System (21) represents the algebraic counterpart of the following variational problem: find $u_{1,\delta} \in V_{1,\delta}$ and $u_{2,\delta} \in V_{2,\delta}$ such that

$$a_1(u_{1,\delta}, v_{1,\delta}) = (f, v_{1,\delta})_{\Omega_1} \quad \forall v_{1,\delta} \in \mathring{V}_{1,\delta}$$

$$a_2(u_{2,\delta}, v_{2,\delta}) = (f, v_{2,\delta})_{\Omega_2} \quad \forall v_{2,\delta} \in \mathring{V}_{2,\delta}$$

$$u_{2,\delta}|_{\Gamma_2} = \Pi_{21}(u_{1,\delta}|_{\Gamma_1}) \tag{22}$$

$$a_1(u_{1,\delta}, w_\delta) + a_2(u_{2,\delta}, \tilde{w}_\delta) = (f, w_\delta)_{\Omega_1} + (f, \tilde{w}_\delta)_{\Omega_2}$$

$$\forall w_\delta \in V_{\Gamma_1}, \ \tilde{w}_\delta = E_2(\Pi_{12}^* w_\delta|_{\Gamma_1}),$$

where $\Pi_{12}^* : \Lambda_{1,\delta} \to \Lambda_{2,\delta}$ is the adjoint operator of Π_{12} w.r.t. the L^2 product, i.e., for any $\eta_{1,\delta} \in \Lambda_{1,\delta}$ and $\eta_{2,\delta} \in \Lambda_{2,\delta}$, it satisfies

$$(\Pi_{12}^* \eta_{1,\delta}, \eta_{2,\delta})_{L^2(\Gamma_2)} = (\eta_{1,\delta}, \Pi_{12} \eta_{2,\delta})_{L^2(\Gamma_1)}. \tag{23}$$

More precisely, $(22)_{1,2}$ correspond to the first two equations of the system (21); $(22)_3$ follows directly by the definition of the space V_{Γ_1} and yields $\mathbf{u}_{\Gamma_2} = Q_{21}\mathbf{u}_{\Gamma_1}$. Finally, $(22)_4$ corresponds to the last equation of system (21). To prove this statement, let us choose $\eta_{2,\delta} = \lambda_j^{(2)}$ (for any $j = 1, \ldots, n_2$) and $\eta_{1,\delta} = \lambda_i^{(1)}$ (for any $i = 1, \ldots, n_1$) in (23), thus by (9) it holds

$$(\Pi_{12}\lambda_j^{(2)})(\mathbf{x}) = \sum_{\ell=1}^{n_1} (\Pi_{12}\lambda_j^{(2)})(\mathbf{x}_\ell^{(\Gamma_1)}) \lambda_\ell^{(1)}(\mathbf{x}) \quad \forall \mathbf{x} \in \Gamma_1,$$

and

$$\begin{aligned}
(\Pi_{12}\lambda_j^{(2)}, \lambda_i^{(1)})_{L^2(\Gamma_1)} &= \int_{\Gamma_1} \sum_{\ell=1}^{n_1} (\Pi_{12}\lambda_j^{(2)})(\mathbf{x}_\ell^{(\Gamma_1)}) \lambda_\ell^{(1)}(\mathbf{x}) \lambda_i^{(1)}(\mathbf{x}) d\Gamma \\
&= \sum_{\ell=1}^{n_1} (\Pi_{12}\lambda_j^{(2)})(\mathbf{x}_\ell^{(\Gamma_1)}) \int_{\Gamma_1} \lambda_\ell^{(1)}(\mathbf{x}) \lambda_i^{(1)}(\mathbf{x}) d\Gamma \\
&= \sum_{\ell=1}^{n_1} (R_{12})_{\ell j} (M_{\Gamma_1})_{i\ell} = (M_{\Gamma_1} R_{12})_{ij}.
\end{aligned}$$

At the same time, if we expand $\Pi_{12}^* \lambda_i^{(1)}$ w.r.t. the basis function in $\Lambda_{2,\delta}$ as

$$(\Pi_{12}^* \lambda_i^{(1)})(\mathbf{x}) = \sum_{k=1}^{n_2} (\Pi_{12}^* \lambda_i^{(1)})(\mathbf{x}_k^{(2)}) \lambda_k^{(\Gamma_2)}(\mathbf{x}) \quad \forall \mathbf{x} \in \Gamma_2, \tag{24}$$

and we denote by P the associated matrix such that $P_{ji} = (\Pi_{12}^* \lambda_i^{(1)})(\mathbf{x}_j^{(\Gamma_2)})$, we have

$$
\begin{aligned}
(\Pi_{12}^* \lambda_i^{(1)}, \lambda_j^{(2)})_{L^2(\Gamma_2)} &= \int_{\Gamma_2} \sum_{k=1}^{n_2} (\Pi_{12}^* \lambda_i^{(1)})(\mathbf{x}_k^{(\Gamma_2)}) \lambda_k^{(2)}(\mathbf{x}) \lambda_j^{(2)}(\mathbf{x}) d\Gamma \\
&= \sum_{k=1}^{n_2} (\Pi_{12}^* \lambda_i^{(1)})(\mathbf{x}_k^{(\Gamma_2)}) \int_{\Gamma_2} \lambda_k^{(2)}(\mathbf{x}) \lambda_j^{(2)}(\mathbf{x}) d\Gamma \\
&= \sum_{k=1}^{n_2} P_{ki} (M_{\Gamma_2})_{jk} = (M_{\Gamma_2} P)_{ji}.
\end{aligned}
$$

Then, the algebraic counterpart of (23) reads

$$
(M_{\Gamma_1} R_{12})_{ij} = (M_{\Gamma_2} P)_{ji} = (P^T M_{\Gamma_2})_{ij},
$$

for any $i = 1, \ldots, n_1$ and $j = 1, \ldots, n_2$, or equivalently

$$
P^T = M_{\Gamma_1} R_{12} M_{\Gamma_2}^{-1} \quad (= Q_{12} \text{ by (20)}).
$$

This means that the matrix associated with Π_{12}^* is $P = Q_{12}^T$.

Now, let us write

$$
\begin{aligned}
u_{1,\delta}(\mathbf{x}) = \ & \sum_{j=1}^{N_1} u_{1,\delta}(\mathbf{x}_j^{(1)}) \Phi_j^{(1)}(\mathbf{x}) \\
& + \sum_{j=1}^{n_1} u_{1,\delta}(\mathbf{x}_j^{(\Gamma_1)}) E_1 \lambda_j^e(\mathbf{x}) \qquad \forall \mathbf{x} \in \overline{\Omega}_1, \\
u_{2,\delta}(\mathbf{x}) = \ & \sum_{j=1}^{N_2} u_{2,\delta}(\mathbf{x}_j^{(2)}) \Phi_j^{(2)}(\mathbf{x}) \\
& + \sum_{j=1}^{n_1} u_{1,\delta}(\mathbf{x}_j^{(\Gamma_1)}) E_2(\Pi_{21} \lambda_j^e)(\mathbf{x}) \qquad \forall \mathbf{x} \in \overline{\Omega}_2,
\end{aligned}
$$

set

$$
\mathbf{u}_k = [u_{k,\delta}(\mathbf{x}_j^{(k)})]_{j=1}^{N_k} \ (k = 1, 2), \quad \mathbf{u}_{\Gamma_1} = [u_{1,\delta}(\mathbf{x}_j^{(\Gamma_1)})]_{j=1}^{n_1},
$$

and choose $w_\delta = \lambda_i^e$, $i = 1, \ldots, n_1$.

Then $(22)_4$ reads

$$
\begin{aligned}
& \sum_{j=1}^{N_1} \mathbf{u}_{1j} a_1(\Phi_j^{(1)}, E_1 \lambda_i^e) + \sum_{j=1}^{N_2} \mathbf{u}_{2j} a_2(\Phi_j^{(2)}, E_2(\Pi_{12}^* \lambda_i^e)) \\
& + \sum_{j=1}^{n_1} \mathbf{u}_{\Gamma_1 j} [a_1(E_1 \lambda_j^e, E_1 \lambda_i^e) + a_2(E_2(\Pi_{21} \lambda_j^e), E_2(\Pi_{12}^* \lambda_i^e)) \\
& = (f, E_1 \lambda_i^e)_{\Omega_1} + (f, E_2(\Pi_{12}^* \lambda_i^e))_{\Omega_2}.
\end{aligned}
$$

Recalling that $\lambda_i^e|_{\Omega_1} = E_1 \lambda_i^{(1)}$, $\lambda_i^e|_{\Omega_2} = E_2(\Pi_{12}^* \lambda_i^{(1)})$, and thanks to both (17) and (24), it holds

$$
\begin{aligned}
a_2(\Phi_j^{(2)}, E_2(\Pi_{12}^* \lambda_i^e)) &= \sum_{k=1}^{n_2} (\Pi_{12}^* \lambda_i^e)(\mathbf{x}_k^{(\Gamma_2)}) a_2(\Phi_j^{(2)}, E_2 \lambda_k^{(2)}) \\
&= \sum_{k=1}^{n_2} (Q_{12}^T)_{ki}(A_{\Gamma_2,2})_{kj} = (Q_{12} A_{\Gamma_2,2})_{ij},
\end{aligned}
$$

$$
\begin{aligned}
a_2(E_2(\Pi_{21} \lambda_j^e), E_2(\Pi_{12}^* \lambda_i^e)) &= \\
&= \sum_{k=1}^{n_2} (\Pi_{12}^* \lambda_i^e)(\mathbf{x}_k^{(\Gamma_2)}) \sum_{\ell=1}^{n_2} (\Pi_{21} \lambda_k^e)(\mathbf{x}_\ell^{(\Gamma_2)}) a_2(E_2 \lambda_\ell^{(2)}, E_2 \lambda_k^{(2)}) \\
&= \sum_{k=1}^{n_2} \sum_{\ell=1}^{n_2} (Q_{12}^T)_{ki}(A_{\Gamma_2,2})_{k\ell}(Q_{21})_{\ell j} = (Q_{12} A_{\Gamma_2,2} Q_{21})_{ij}.
\end{aligned}
$$

and

$$
(f, E_2(\Pi_{12}^* \lambda_i^e))_{\Omega_2} = (Q_{12} \mathbf{f}_{\Gamma_2})_i,
$$

thus $(21)_3$ is the algebraic counterpart of $(22)_4$.

Equation $(22)_4$ (or equivalently $(21)_3$) expresses the balance of residuals in strong form. Algebraically, this becomes more evident once we reformulate $(21)_3$ as

$$
-Q_{12}\mathbf{r}_2 = -M_{\Gamma_1} R_{12} M_{\Gamma_2}^{-1} \mathbf{r}_2 = \mathbf{r}_1, \tag{25}
$$

where

$$
\mathbf{r}_k = \mathbf{f}_k - A_{\Gamma_k,k}\mathbf{u}_k - A_{\Gamma_k,\Gamma_k}\mathbf{u}_{\Gamma_k}. \tag{26}
$$

In eq. (25), we notice that $M_{\Gamma_2}^{-1}\mathbf{r}_2$ is an approximation of the strong form of the normal stresses on Γ_2; $R_{12} M_{\Gamma_2}^{-1}\mathbf{r}_2$ is an interpolation of the normal stresses on Γ_1, still in strong form, and $M_{\Gamma_1} R_{12} M_{\Gamma_2}^{-1}\mathbf{r}_2$ returns the weak form of the normal stresses but now on Γ_1. Note that the order of magnitude of the entries of $\mathbf{r}_2$ depend on the mesh size used to discretize Ω_2, that of the entries of $\mathbf{r}_1$ depend on the mesh size of Ω_1, while the order of magnitude of those of both $M_{\Gamma_2}^{-1}\mathbf{r}_2$ and $R_{12} M_{\Gamma_2}^{-1}\mathbf{r}_2$ are independent of the mesh size.

Remark 5.1. *In the conforming case, by setting $\Pi_{12} = \Pi_{21} = I$, Eq. $(22)_3$ returns the well known two-domain formulation associated with the Galerkin finite element method, see [18].*

By defining the spaces

$$V_{\Gamma_1}^* = \{\varphi^* * \in L^2(\Omega) : \exists \lambda_1 \in \Lambda_{1,\delta} : \quad \varphi^*|_{\Omega_1} = E_1 \lambda_1, \\ \varphi^*|_{\Omega_2} = E_2(\Pi_{12}^* \lambda_1)\}. \tag{27}$$

and

$$V_\delta^* = \mathring{V}_{1,\delta} \oplus \mathring{V}_{2,\delta} \oplus V_{\Gamma_1}^*, \tag{28}$$

the variational statement (22) can be written in compact form as a *non-conforming Petrov-Galerkin* problem: find $u_\delta \in V_\delta$:

$$a_1(u_\delta, v_\delta^*) + a_2(u_\delta, v_\delta^*) = (f, v_\delta^*)_{\Omega_1} + (f, v_\delta^*)_{\Omega_2}, \quad \forall v_\delta^* \in V_\delta^*. \tag{29}$$

In order to reformulate (29) as a (more convenient) *non-conforming generalized Galerkin* problem, for any $w_\delta \in V_\delta$ we define

$$a_{2,\delta}(w_\delta, v_\delta) = \begin{cases} a_2(w_\delta, v_\delta), & \text{if } v_\delta \in \mathring{V}_{1,\delta} \oplus \mathring{V}_{2,\delta} \\ a_2(w_\delta, E_2(\Pi_{12}^* v_\delta|_{\Gamma_1})), & \text{if } v_\delta \in V_{\Gamma_1} \end{cases}$$

$$\tag{30}$$

$$(f, v_\delta)_{2,\delta} = \begin{cases} (f, v_\delta)_{\Omega_2}, & \text{if } v_\delta \in \mathring{V}_{1,\delta} \oplus \mathring{V}_{2,\delta} \\ (f, E_2(\Pi_{12}^* v_\delta|_{\Gamma_1}))_{\Omega_2}, & \text{if } v_\delta \in V_{\Gamma_1}. \end{cases}$$

Then (22) is equivalently reformulated as a non-conforming generalized Galerkin problem: look for $u_\delta \in V_\delta$:

$$a_1(u_\delta, v_\delta) + a_{2,\delta}(u_\delta, v_\delta) = (f, v_\delta)_{\Omega_1} + (f, v_\delta)_{2,\delta}, \quad \forall v_\delta \in V_\delta. \tag{31}$$

Remark 5.2 (Dirichlet condition on $\Gamma \cap \partial\Omega_D$). *The special case where a Dirichlet condition is set at a point $P \in \Gamma \cap \partial\Omega_D$ (e.g. the case of Fig. 1, right) has to be treated with a grain of salt. Equation (31) tested on the basis function $v_\delta = \lambda_P^e$ needs to be completed as follows:*

$$a_1(u_\delta, \lambda_P^e) + a_{2,\delta}(u_\delta, \lambda_P^e) = (f, \lambda_P^e)_{\Omega_1} + (f, \lambda_P^e)_{2,\delta} + \int_{\partial\Omega_D} \mu \frac{\partial u_\delta}{\partial n} \lambda_P^e. \tag{32}$$

5.2. On the mortar method

In spite of the fact that the mortar method is a projection (rather than an interpolation-based) method, we are still able to cast it into the general form (21). For that, it is enough to replace Q_{21} with the matrix associated with the mortar projection (named Ξ in [16, Sect. 11.4]) and Q_{12} with Q_{21}^T.

Similarly, the variational formulation of the mortar method (see [4]) can be retrieved from (31) by replacing V_δ with the mortar space

$$V_\delta^M = \{v_\delta \in L^2(\Omega), v_{k,\delta} = v_\delta|_{\Omega_k} \in V_{k,\delta} \text{ for } k = 1, 2 \text{ and} \atop v_{2,\delta} = \Pi_{21}^M v_{1,\delta} \text{ on } \Gamma\}, \tag{33}$$

where Π_{21}^M is the L^2-projection from the master to the slave on the interface, and by identifying Π_{12}^* with Π_{21}^M in (30).

We warn the reader that our method *does not* coincide with the pointwise matching presented in [4, eq. (3.7)] (which is notoriously sub-optimal).

The implementation of mortar based methods (in particular in 3D) is rather involved. This is due for instance to the need of numerically evaluating either cross-grid mass-matrices and, in case of non-conforming interfaces, normal projections between meshes. This is not the case for the proposed method; in particular, the RL-RBF can treat the case of geometrically non-conforming interfaces.

6. Numerical solution of an elliptic problem

In the first preliminary test, we consider the numerical solution of the Poisson problem

$$-\Delta u(x,y) = f(x,y) \quad \text{in} \quad \Omega = (0,2) \times (0,1), \tag{34}$$
$$u(x,y) = g(x,y) \quad \text{on} \quad \partial\Omega,$$

in two-dimensions and we show the orders of convergence of INTERNODES when non-conforming meshes and/or non-conforming discretizations (based on the coupling of finite elements with spectral elements) are used.

In (34) the functions $f(x,y)$ and $g(x,y)$ are chosen such that $u(x,y) = \arctan(4(y-0.5)) \cos(\pi x)$. We decompose the domain Ω in two subdomains: $\Omega_1 = (0,1) \times (0,1)$ and $\Omega_2 = (1,2) \times (0,1)$.

6.1. Coupling of non-conforming FEM-FEM discretizations

In this Section we solve problem (34) by considering non-conforming finite elements discretizations at the subdomains interface Γ. The non-conformity may come from the use of different mesh-sizes and/or different orders of finite elements basis functions between the master and slave domains. In our numerical experiments we considered $\mathbb{P}_1, \mathbb{P}_2$ and $\mathbb{P}_3$ finite elements, using structured grids that feature an aspect ratio of 1 or 2 across the interface. Furthermore, the method proposed is tested using both the Lagrange and the RL-RBF interpolants as intergrid operator.
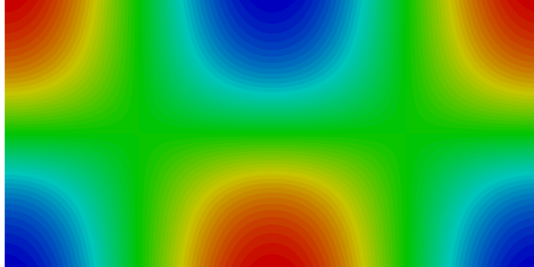
Figure 4: Solution $u(x, y) = \arctan(4(y - 0.5)) \cos(\pi x)$ of problem (34).

In Figure 5 we show the rate of convergence obtained by INTERNODES for some of the simulations performed using the Lagrange interpolant and for an aspect ratio between the master and slave grids roughly equal to 2: the pictures in the left column refer to the case of a fine-master and coarse-slave meshes, while those in the right column to the opposite case. The results reported are the H^1-norms of the errors computed in each individual subdomain, i.e., $\|u - u_{1,\delta}\|_{H^1(\Omega_1)}$ and $\|u - u_{2,\delta}\|_{H^1(\Omega_2)}$.

By comparing the left and right plots in the first and fourth rows of Figure 5 (obtained with non-conforming meshes but same polynomial degree in the master and slave domains) we observe that, as expected, the most accurate results are always obtained on the subdomain triangulated with the finer mesh, independently whether this is a master or a slave. When the master domain is discretized using a polynomial degree lower than the one of the slave (compare the left and right plots of the second row in Figure 5) we notice that it is better, in terms of accuracy, to use the finer mesh on the master domain. In the opposite case, i.e. when the master domain is discretized using a polynomial degree that is higher than the one of the slave (compare the left and right plots of the third row in Figure 5) we observe that more precise results are obtained using the finer mesh on the slave domain.

In Table 1 we summarize the orders of convergence obtained by IN-TERNODES using non-conforming meshes and the Lagrange interpolant, while in Table 3 those using matching grids but non-conforming polynomial degrees. Let us denote by p_1 and p_2 the polynomial degrees used in Ω_1 and Ω_2, respectively. As shown in Table 1, if $|p_1 - p_2| \leq 1$, the use of the Lagrange interpolant yields rates of convergence that are optimal in each individual subdomain, in fact they behave as $h_i^{p_i}$, independently of the choice of which domain plays the role of the master or slave. In the case where
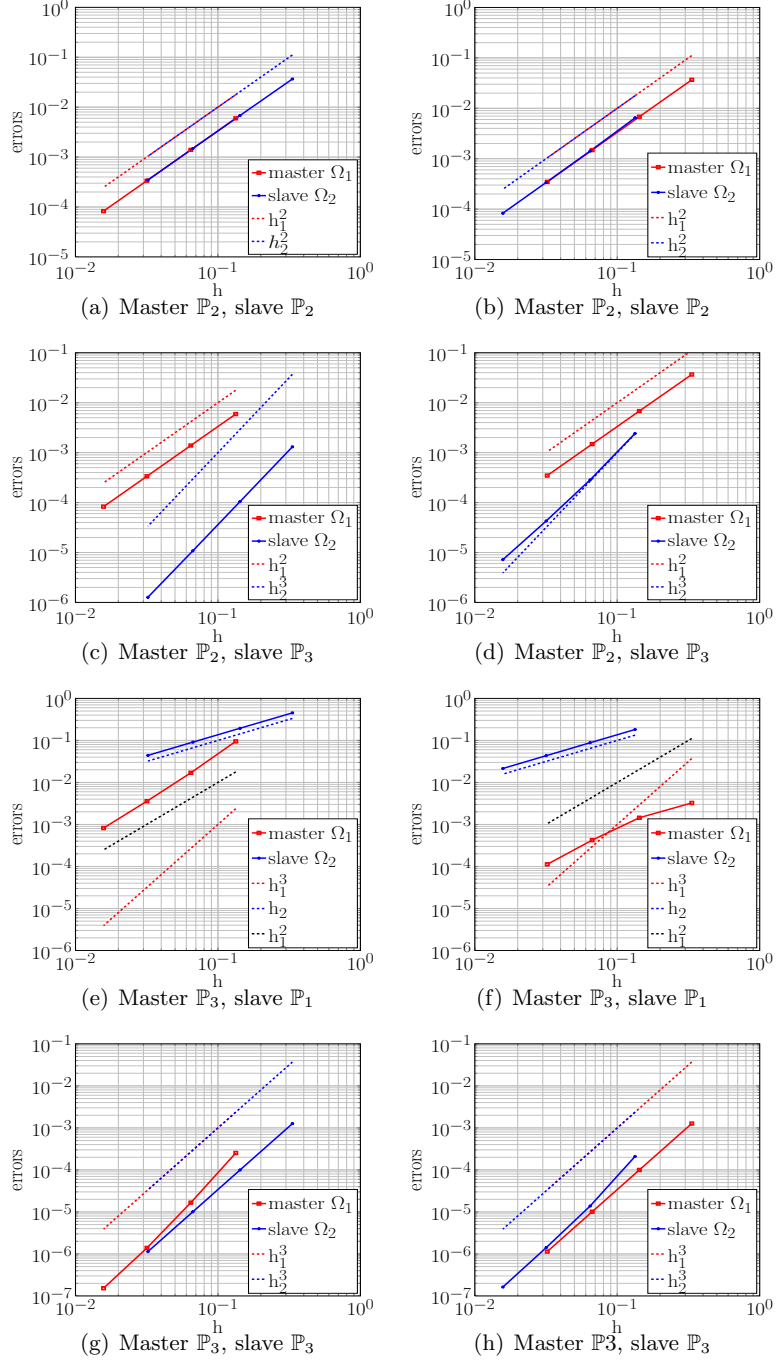
15

Figure 5: FEM-FEM coupling: orders of convergence obtained using Lagrangian interpolants and non-conforming meshes with aspect ratio 2. Left: master with finer mesh, slave coarser; right: vice versa.

16

Master \ Slave	$\mathbb{P}_1$		$\mathbb{P}_2$		$\mathbb{P}_3$	
$\mathbb{P}_1$	1-1	1-1	1-2	1-2	1-1	1-1
	1-1	1-1	1-2	1-2	1-1	1-1
$\mathbb{P}_2$	2-1	2-1	2-2	2-2	2-3	2-3
	2-1	2-1	2-2	2-2	2-3	2-3
$\mathbb{P}_3$	2-1	2-1	3-2	3-2	3-3	3-3
	2-1	2-1	3-2	3-2	3-3	3-3

Table 1: Orders of convergence in H^1 norm obtained using non-conforming meshes and the Lagrange interpolation. In the top row we report the results obtained using aspect ratio roughly equal to 1 between the master and slave grids while in the bottom those with aspect ratio roughly equal to 2. On the left column a finer mesh is used in the master domain and a coarse one in the slave domain while on the right column it is the opposite.

Master \ Slave	$\mathbb{P}_1$		$\mathbb{P}_2$		$\mathbb{P}_3$	
$\mathbb{P}_1$	1-1	1-1	1-2	1-2	1-2	1-2
	1-1	1-1	1-2	1-2	1-2	1-2
$\mathbb{P}_2$	2-1	2-1	2-2	2-2	2-3	2-3
	2-1	2-1	2-2	2-2	2-3	2-3
$\mathbb{P}_3$	2-1	2-1	3-2	3-2	3-3	3-3
	2-1	2-1	3-2	3-2	3-3	2-2

Table 2: Orders of convergence in H^1 norm obtained using non-conforming meshes and the RL-RBF interpolation. The cells are organized as in Table 1.

$p_1 - p_2 > 1$, for instance using $\mathbb{P}_3$-$\mathbb{P}_1$ finite elements, the rate of convergence behaves like $h_1^{p_1-1}$ in Ω_1 and like $h_2^{p_2}$ in Ω_2 (or, if $p_2 - p_1 > 1$, as $h_1^{p_1}$ in Ω_1 and as $h_2^{p_1+1}$ in Ω_2).

In Table 2 the results obtained on non-conforming meshes using the RL-RBF interpolant are reported. We notice that, if $|p_1 - p_2| \leq 1$, the method leads to optimal rates of convergence in all the numerical experiments performed a part from the case of the $\mathbb{P}_3$-$\mathbb{P}_3$ discretization with grids featuring aspect ratio roughly equal to 2. This may be due to the fact that, as shown in Eq. (12), the construction of the RL-RBF interpolant does not take into account the polynomial degree of the trace of the finite element basis functions at the interface since it only depends on the values at the interface grid points.

However, this makes RL-RBF a flexible interpolation tool to deal with problems in which the subdomains feature geometrically non-conforming

M \ S	$\mathbb{P}_1$		$\mathbb{P}_2$		$\mathbb{P}_3$	
$\mathbb{P}_1$	1-1	1-1	1-2	1-2	1-2	1-2
$\mathbb{P}_2$	2-1	2-1	2-2	2-2	2-3	2-3
$\mathbb{P}_3$	2-1	2-1	3-2	3-2	3-3	3-3

Table 3: Orders of convergence in H^1 norm obtained using conforming meshes but non-conforming Finite Element discretizations. In each cell of the table, on the left we and the on the right we report the results computed using the Lagrange and the RL-RBF interpolant, respectively. M stands for master while S for slave domain.

interfaces (as in the case of Figure 3). In fact, due to the use of a local radius of support of the radial basis functions [7], the geometrically non-conforming case can be easily handled without any additional projection that is typically used in this case to retrieve geometrically conforming interfaces, cf. [8, 13].

6.2. Coupling of non-conforming SEM-SEM discretizations

In this Section we consider SEM discretization in both master and slave domains and we compare the errors obtained by INTERNODES (using the Lagrange intergrid operator) with those generated by the mortar approach. As in the previous subsection, we plot the errors in H^1-norm, i.e., $\|u - u_{1,\delta}\|_{H^1(\Omega_1)}$ and $\|u - u_{2,\delta}\|_{H^1(\Omega_2)}$.

Pictures in the left column of Figure 6 refer to INTERNODES, while those in the right column to the mortar approach.

Let p_1 and p_2 denote the polynomial degrees used in Ω_1 and Ω_2, respectively. The errors displayed by the two methods are comparable; moreover, for $i = 1, 2$, they decay as $h_i^{p_i}$ if $|p_1 - p_2| \leq 1$, while the order of convergence is downgraded when $|p_1 - p_2| > 1$, as we can see in the last row of Figure 6, where $p_1 = 5$ and $p_2 = 2$. In fact, in the latter case, the error in the master domain behaves like h_1^3 for both the methods and not as h_1^5.

More precisely, the plot in the first row refers to a test case with polynomial conformity and mesh non-conformity with aspect ratio $h_1/h_2 \simeq 2$; the one in the second row to a case with both polynomial and mesh non-conformity, with $h_1/h_2 \simeq 1/2$ and $p_1 = p_2 + 1$; that in the third row again to a case with both polynomial and mesh non-conformity, with $h_1/h_2 \simeq 1/2$ and $p_1 = p_2 - 1$; finally the last row to a situation with $p_1 - p_2 > 1$, $h_1 < h_2$, and $h_1/h_2 \simeq 1$.

In Tables 4 and 5 we show the rates of convergence with respect to h both for our method and the mortar approach, respectively, when considering different non-conforming situations, as those in Tables 1 and 2.

First of all we notice that INTERNODES is accurate as well as the mortar and does not suffer of sub-optimal convergence as the pointwise matching presented in [4, eq (3.7)]. Furthermore, the trend observed for the FEM discretization (and anticipated by the convergence curves of Figure 6) holds also for SEM case.

M \ S	$\mathbb{Q}_2$		$\mathbb{Q}_3$		$\mathbb{Q}_4$		$\mathbb{Q}_5$	
$\mathbb{Q}_2$	2-2	2-2	2-3	2-3	2-2	2-3	2-2	2-3
	2-2	2-2	2-3	2-3	2-2	2-3	2-2	2-3
$\mathbb{Q}_3$	3-2	3-2	3-3	3-3	3-4	3-4	3-3	3-4
	3-2	3-2	3-3	3-3	3-4	3-4	3-4	3-4
$\mathbb{Q}_4$	4-2	3-2	4-3	4-3	4-4	4-4	4-5	4-5
	3-2	3-2	4-3	4-3	4-4	4-4	4-5	4-5
$\mathbb{Q}_5$	4-2	3-2	5-3	4-3	5-4	5-4	5-5	5-5
	3-2	3-2	5-3	5-3	5-4	5-4	5-5	5-5

Table 4: SEM-SEM coupling: orders of convergence of INTERNODES using non-conforming meshes. M stands for master domain while S for slave domain. The cells are organized as in Table 1.

M \ S	$\mathbb{Q}_2$		$\mathbb{Q}_3$		$\mathbb{Q}_4$		$\mathbb{Q}_5$	
$\mathbb{Q}_2$	2-2	2-2	2-3	2-3	2-2	2-3	2-2	2-3
	2-2	2-2	2-3	2-3	2-2	2-3	2-2	2-3
$\mathbb{Q}_3$	3-2	3-2	3-3	3-3	3-4	3-4	3-3	3-4
	3-2	3-2	3-3	3-3	3-4	3-4	3-4	3-4
$\mathbb{Q}_4$	4-2	3-2	4-3	4-3	4-4	4-4	4-5	4-5
	3-2	3-2	4-3	4-3	4-4	4-4	4-5	4-5
$\mathbb{Q}_5$	4-2	3-2	5-3	4-3	5-4	5-4	5-5	5-5
	3-2	3-2	5-3	5-3	5-4	5-4	5-5	5-5

Table 5: SEM-SEM coupling: orders of convergence of the mortar approach using non-conforming meshes. M stands for master domain while S for slave domain. The cells are organized as in Table 1.

In Table 6 the orders of convergence in H^1 norm versus the mesh size h are shown in the case of conforming meshes and different (but also equal) polynomial degrees.
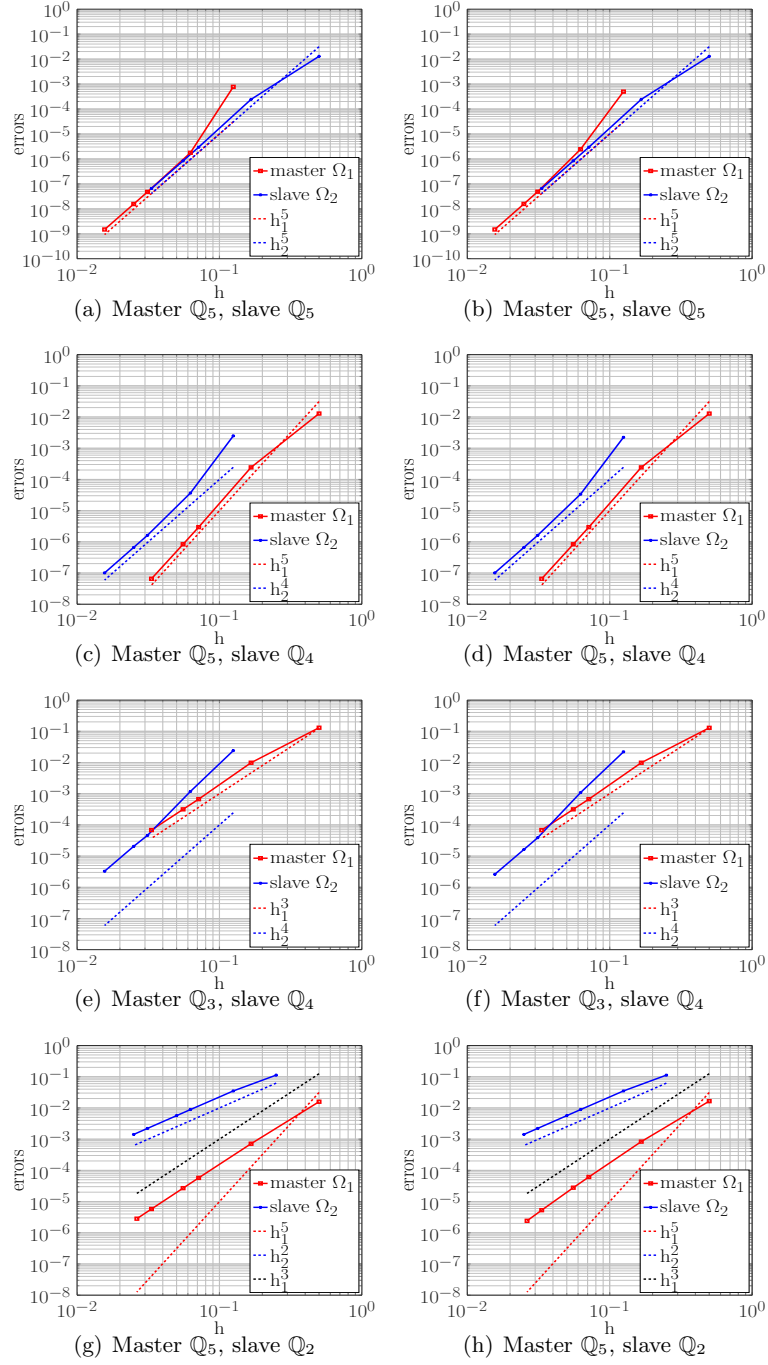
Figure 6: Convergence history w.r.t. h for INTERNODES (left) and mortar (right) approaches. SEM discretization. Top line: $h_1/h_2 \simeq 2$; second line: $h_1/h_2 \simeq 1/2$; third line: $h_1/h_2 \simeq 1/2$; fourth line: $h_1 < h_2$, $h_1/h_2 \simeq 1$. Left: master coarse, slave fine; right: vice versa.

20

M \ S	$\mathbb{Q}_2$		$\mathbb{Q}_3$		$\mathbb{Q}_4$		$\mathbb{Q}_5$	
$\mathbb{Q}_2$	2-2	2-2	2-3	2-3	2-2	2-2	2-2	2-2
$\mathbb{Q}_3$	3-2	3-2	3-3	3-3	3-4	3-4	3-4	3-4
$\mathbb{Q}_4$	4-2	4-2	4-3	4-3	4-4	4-4	4-5	4-5
$\mathbb{Q}_5$	4-2	4-2	5-3	5-3	5-4	5-4	5-5	5-5

Table 6: SEM-SEM coupling: orders of convergence with respect to h, using conforming meshes. In each cell of the table, on the left and on the right we report the results computed using INTERNODES and mortar approach, respectively.

6.3. Coupling of FEM-SEM discretizations

We consider now the coupling of FEM-SEM discretizations. We set $\Omega_1 = (0,1) \times (0,1)$, $\Omega_2 = (1,2) \times (0,1)$ and the function $u(x,y) = \arctan(4(y - 0.5))\cos(\pi(x - 0.1))$ as exact solution of the problem (34).

Polynomial non-conformity. In Table 7 we show the convergence orders w.r.t. the mesh size h when the master domain Ω_1 is discretized by $\mathbb{P}_1$ finite elements and the slave domain Ω_2 by $\mathbb{Q}_p$ spectral elements with $p = 2, 3, 4$ and vice versa. h denotes the diameter of the structured and regular triangular mesh, that coincides with the diameter of the spectral elements. In this first test case we consider mesh conformity and interpolation by either Lagrange and RL-RBF. Finally we compare the results obtained by INTERNODES with those generated by the mortar method.

The advantage of using RL-RBF instead of Lagrange interpolation is clear when the master discrete space is the poorest one, i.e. when it is discretized by $\mathbb{P}_1$. More precisely, when using Lagrange interpolation, the first order of convergence driven by $\mathbb{P}_1$ in Ω_1 is observed in Ω_2 as well, even if in Ω_2 a higher degree, $p \geq 2$, is used. Conversely, when using RL-RBF, the order of convergence in the slave domain is equal to 2, thus reflecting the more accurate discretization used. In any case, even when $p > 2$ the order of convergence in Ω_2 is still 2.

When the master domain is discretized more finely by $\mathbb{Q}_p$ ($p \geq 2$) and $\mathbb{P}_1$ are used in the slave, the rates of convergence are 2 and 1 in the master and the slave domain, respectively, for both the approaches.

Mesh non-conformity. We consider now non-conforming meshes and, as in the previous sections, four different situations, characterized by a varying aspect ratio between the mesh sizes h_1 and h_2, as well as by the refinements of the grids. In Tables 8 and 9 the convergence orders w.r.t. the mesh size h are shown. As for the mesh conforming case, when the master domain is

Master - Slave	Lagrange	RL-RBF	mortar
$\mathbb{P}_1 - \mathbb{Q}_2$	1-1	1-2	1-1.6
$\mathbb{P}_1 - \mathbb{Q}_3$	1-1	1-2	1-1.7
$\mathbb{P}_1 - \mathbb{Q}_4$	1-1	1-2	1-1.7
$\mathbb{Q}_2 - \mathbb{P}_1$	2-1	2-1	2-1
$\mathbb{Q}_3 - \mathbb{P}_1$	2-1	2-1	2-1
$\mathbb{Q}_4 - \mathbb{P}_1$	2-1	2-1	2-1

Table 7: FEM-SEM coupling: orders of convergence w.r.t. the mesh-size h when using conforming meshes.

discretized by $\mathbb{P}_1$, the Lagrange interpolation downgrades the higher approximation degree of the slave domain, while the RL-RBF interpolation always provides convergence order 1 in the master domain and 2 in the slave one. On the contrary, when the master domain is discretized by SEM, the convergence orders w.r.t. h are 2 in the master domain and 1 in the slave one for all the considered approaches.

Master - Slave	Lagrange		RL-RBF		mortar	
$\mathbb{P}_1 - \mathbb{Q}_2$	1-1.5	1-2	1-2	1-2	1-2	1-2
	1-2	1-1.5	1-2	1-2	1-2	1-2
$\mathbb{P}_1 - \mathbb{Q}_3$	1-1	1-2	1-2	1-2	1-1.5	1-2
	1-1	1-1.5	1-2	1-2	1-2	1-2
$\mathbb{P}_1 - \mathbb{Q}_4$	1-1	1-2	1-2	1-2	1-1.5	1-2
	1-1	1-1	1-2	1-2	1-2	1-2

Table 8: FEM-SEM coupling: orders of convergence w.r.t. the mesh-sizes h_1 in Ω_1 and h_2 in Ω_2 when using non-conforming meshes. The cells are organized as in Table 1.

It is clear that the higher accuracy of the SEM discretization is downgraded by that of the $\mathbb{P}_1$ FEM approximation. To validate such conjecture, we fix now the discretization in Ω_1 (master domain) by using 6×6 quads $\mathbb{Q}_4$, while we refine the $\mathbb{P}_1$ mesh in Ω_2 by choosing $h_2 = 1/8$, $1/16$, $1/32$, $1/64$, $1/128$. In Figure 7, the H^1 norm of the errors with respect to the exact solution are shown versus h_2. The error in Ω_1 decays as h_2^2 until the accuracy prescribed by global $\mathbb{Q}_4$ discretization is reached, while the error in Ω_2 is $\mathcal{O}(h_2)$. In Figure 8 we show the meshes used and contours of the computed solutions when $h_2 = 1/8$ and $h_2 = 1/32$. The rough approximation around the interface is evident when $h_2 = 1/8$.
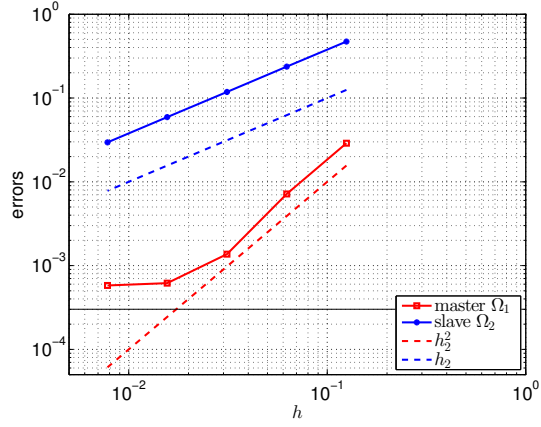
Figure 7: SEM-FEM coupling. H^1 norm errors vs. h_2 when $\mathbb{Q}_4$ are used in Ω_1 (master) with fix $h_1 = 1/6$, and $\mathbb{P}_1$ are used in Ω_2 (slave). The black line denotes the error obtained by discretizing the global domain by conforming $\mathbb{Q}_4$ SEM.
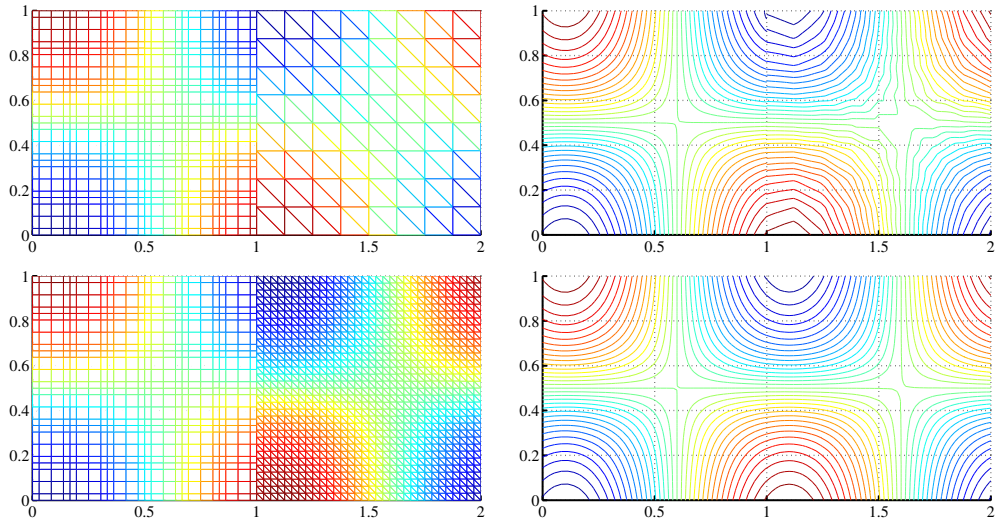

Figure 8: SEM-FEM coupling. Meshes (at left) and solution contours (at right) obtained using $\mathbb{Q}_4$ in Ω_1 (master) and $\mathbb{P}_1$ in Ω_2 (slave). At top $h_2 = 1/8$, at bottom $h_2 = 1/32$.

Master - Slave	Lagrange		RL-RBF		mortar	
$\mathbb{Q}_2 - \mathbb{P}_1$	2-1	2-1	2-1	2-1	2-1	2-1
	2-1	2-1	2-1	2-1	2-1	2-1
$\mathbb{Q}_3 - \mathbb{P}_1$	2-1	2-1	2-1	2-1	2-1	2-1
	2-1	2-1	2-1	2-1	2-1	2-1
$\mathbb{Q}_4 - \mathbb{P}_1$	2-1	2-1	2-1	2-1	2-1	2-1
	2-1	2-1	2-1	2-1	2-1	2-1

Table 9: SEM-FEM coupling: orders of convergence w.r.t. the respective mesh-sizes h_1 in Ω_1 and h_2 in Ω_2 when using non-conforming meshes. The cells are organized as in Table 1.

6.4. On the orders of convergence of INTERNODES

All the numerical convergence results reported before can be summarized by the following empirical formula: if both h_1, $h_2 \to 0$

$$\|u - u_{i,\delta}\|_{H^1(\Omega_i)} \leq C_i(p_1, p_2) h_i^{\min(q_i, s_i - 1)} \|u\|_{H^{s_i}(\Omega_i)} \quad \text{for } i = 1, 2, \qquad (35)$$

where

$$
\begin{aligned}
q_1 &= \min(p_1, p_2 + 1), \\
q_2 &= \begin{cases} p_2 & \text{if } p_2 \leq p_1 + 1 \\ p_1 & \text{if } p_2 > p_1 + 1. \end{cases}
\end{aligned}
$$

In (35), C_i are positive constants independent of h_i, while $s_i > 1$ is the order of the Sobolev regularity of the exact solution in Ω_i.

The convergence analysis w.r.t. the polynomial degrees p_i is more involved and it is under investigation. Here, we only remark that the errors $e_i = \|u - u_{i,\delta_i}\|_{H^1(\Omega_i)}$ reflect the typical behaviour observed by SEM approximation (i.e. exponential dependency on the regularity of the exact solution) if both p_i increase and h_i vanish in a comparable way, and provided that the interpolation error across the interface does not affect the consistency error. Furthermore, we notice that in general the errors e_i in each subdomain are not independent, but they affect mutually: in particular we observe that the worst discretization used may be responsible for the sub-optimality convergence in the other domain.

7. Coupling of geometrically non-conforming subdomains

To assess the robustness of INTERNODES with respect to the geometrically non-conforming case, we solve problem (34) with exact solution

$u(x, y) = \sin((x - 1.2)(y - 1.2)2\pi) + 1$ in the domain $\Omega = (-0.5, 0.5) \times (-0.5, 0.5)$, decomposed as shown in Figure 9. The inner circle is centered at point $(0, 0)$ and has radius $R = 0.35$.
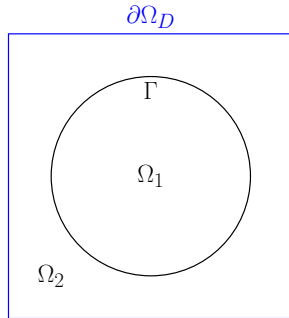

Figure 9: Domain decomposition considered for the example with geometrically non-conforming interfaces.

In Figure 10 we show the results obtained using $\mathbb{P}_1$ finite elements in both the slave and the master domains. Although many gaps and overlaps are present at the interface between the subdomain grids (see bottom row in Figure 10), we observe that the quality of the numerical solutions obtained does not worsen. In Figure 11 the results obtained using first or second order polynomials in the master and slave domains are reported. From Figure 11(a) we observe that when using first order basis functions, INTERNODES leads to first order rate of convergence in both the master and the slave subdomains. Finally, as shown in Figure 11(b), we notice that quadratic convergence is obtained with $\mathbb{P}_2$ finite elements only for sufficiently small mesh sizes for which the gaps and overlaps between the master and slave subdomains tend to become imperceptible (see bottom-right picture of Figure 10).

8. Diffusion of the pollutant around an industrial chimney

We consider now the 2D numerical simulation of the diffusion of the pollutant concentration $u(\mathbf{x})$ in a bounded region around an industrial chimney. To this aim we solve the problem (1) in $\Omega = (0, 1)^2$, with constant diffusion coefficient $\mu = 10^{-3}$, null reaction coefficient α and chimney discharge $f = \chi_\omega$, being χ_ω the characteristic function of the set $\omega = \{\mathbf{x} \in \mathbb{R}^2 : |\mathbf{x} - \mathbf{x}_c| < 0.02\}$ and $\mathbf{x}_c = (0.5, 0.5)$. Homogeneous boundary conditions are set on the boundary $\partial\Omega$.
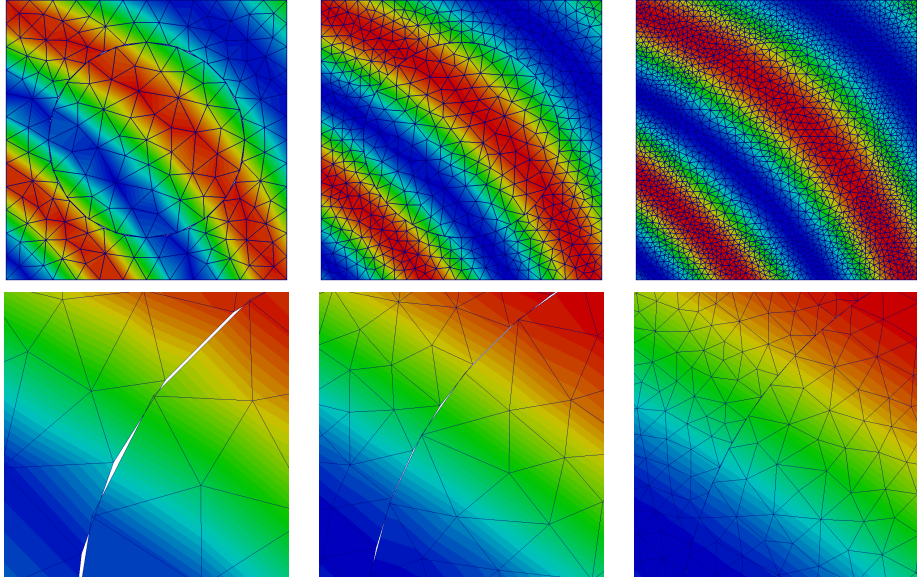
Figure 10: Solutions obtained using $\mathbb{P}_1$-$\mathbb{P}_1$ finite elements for the master and slave domains using meshes of increasing refinement that are geometrically non-conforming. In the top row we show the numerical results on the whole domain while in the bottom row a zoom of the solution close to the interface.
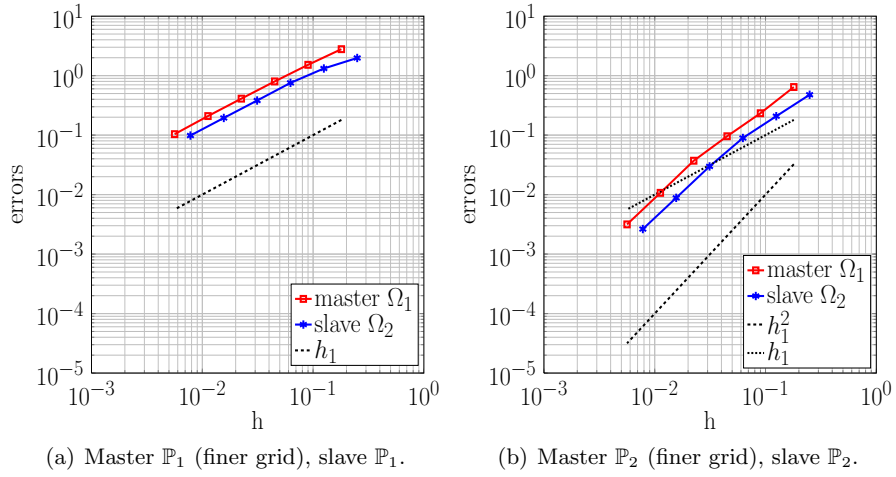

(a) Master $\mathbb{P}_1$ (finer grid), slave $\mathbb{P}_1$.

(b) Master $\mathbb{P}_2$ (finer grid), slave $\mathbb{P}_2$.

Figure 11: Rates of convergence in H^1 norm using geometrically non-conforming interfaces.

26

Since the largest variation of the solution occurs in a small region around the set ω, the computational domain Ω is split into the subsets $\Omega_2 = (0.45, 0.55)^2$ and $\Omega_1 = \Omega \setminus \Omega_2$, then independent meshes are designed there, with the aim to better approximate the solution in proximity of the chimney position. More precisely, 5×5 quads $\mathbb{Q}_8$ are used in Ω_2 (for a total amount of 1681 degrees of freedoms) and $\mathbb{P}_1$ FEM with $h_{max} = 1/20$ in Ω_1 (711 d.o.f and 1331 triangles).

INTERNODES is used to compute the numerical solution, using either the Lagrange or the RL-RBF interpolants as intergrid operators.

We set the external domain Ω_1 to play the role of master, since the other choice (Ω_2 master) would yield a singular problem, in view of the fact that the reaction coefficient α is null and $\partial\Omega_2 = \Gamma_2$ is sctrictly internal to Ω.

In Figure 12 we plot both the mesh (top) and the pollutant concentration (bottom left) obtained by solving problem (1) by INTERNODES method with Lagrange interpolation at the interfaces. The plot at bottom right of Figure 12 refers to the numerical solution obtained by conforming SEM on a uniform mesh of 8×8 quads in Ω with polynomial degree $p = 32$. The range of the color bars used to plot the two numerical solutions is the same, the black box marks the interface Γ between the two subdomans.

In Figure 13 we plot the traces along Γ of the numerical solutions $u_{1,\delta}$ and $u_{2,\delta}$ shown in Figure 12 bottom-left, as well as the trace of the monodomain SEM solution u_{SEM} of Figure 12 bottom-right. The curves are plotted versus the curvilinear abscissa s that starts from the point $(0.45, 0.45)$ and moves counterclockwise along Γ.

9. Numerical solution of a fluid flow past a cylinder

In this Section we consider the numerical simulation of a fluid flow past a cylindrical obstacle at two different Reynolds numbers, that are $Re = 20$ and $Re = 100$, see [20].

We model the flow dynamics by the Navier-Stokes equations for an incompressible fluid. The equations are discretized in space by means of the Finite Element method and in time by Finite Differences. More specifically, we use $\mathbb{P}_1$-$\mathbb{P}_1$ finite elements for the spatial approximation of the fluid velocity and pressure variables (stabilized by SUPG), respectively, while a second order backward differentiation formula is used for the time discretization. The nonlinear convective term in the fluid momentum equation is linearized by means of a second order temporal extrapolation [10, 11].

In order to compare the numerical results obtained by INTERNODES with those available in literature we compute the drag and lift coefficients
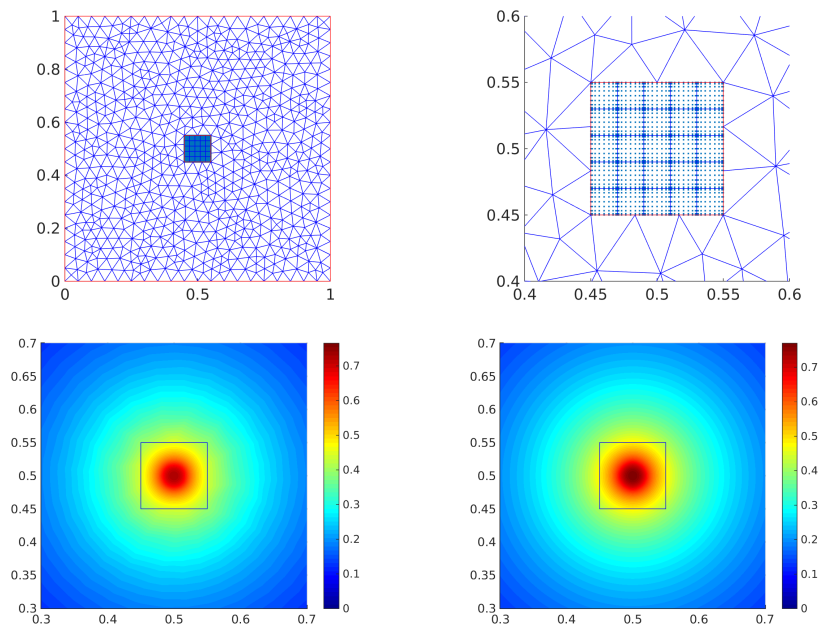
27

Figure 12: At top, the mesh used in the simulation of the diffusion of pollutant concentration (the right picture is a zoom of the left one). At bottom, the numerical solution obtained by both the INTERNODES with Lagrange interpolant as intergrid operator (at left) and by monodomain conforming SEM $\mathbb{Q}_{32}$ on the whole Ω (at right)

of the cylinder. To this end, we introduce a unit vector directed as the incoming flow $\hat{\mathbf{v}}_\infty = \dfrac{\mathbf{v}_\infty}{\|V_\infty\|}$, and a unit vector $\hat{\mathbf{n}}_\infty$ orthogonal to $\hat{\mathbf{v}}_\infty$. The aerodynamic drag and lift coefficients for the cylinder read:

$$C_D(\mathbf{u}, p) = -\frac{1}{q_\infty S} \oint_S (\boldsymbol{\sigma}_f(\mathbf{u}, p)\,\hat{\mathbf{n}}) \cdot \hat{\mathbf{v}}_\infty\, d\Gamma, \qquad (36)$$

$$C_L(\mathbf{u}, p) = \frac{1}{q_\infty S} \oint_S (\boldsymbol{\sigma}_f(\mathbf{u}, p)\,\hat{\mathbf{n}}) \cdot \hat{\mathbf{n}}_\infty\, d\Gamma, \qquad (37)$$

where $\mathbf{u}$ and p are the velocity and pressure variables, $\boldsymbol{\sigma}_f$ is the Cauchy stress tensor of the fluid, $q_\infty = \frac{1}{2}\rho V_\infty^2$ is the dynamic pressure, ρ is the density of the fluid and S is the surface area of the cylinder.

It is well known that for an accurate estimation of the aerodynamic coefficients, the use of a boundary layer refinement of the computational mesh around the cylinder is mandatory. Among the possible strategies to
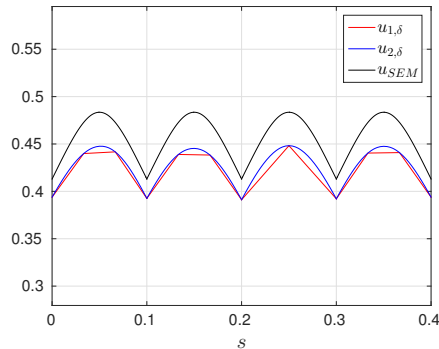
28

Figure 13: Traces of the numerical solutions plotted in Figure 12 versus the curvilinear abscissa s that starts from the point $(0.45, 0.45)$ and moves counterclockwise along Γ.

generate such a refinement, one consists in gradually decreasing the mesh element size in the domain while approaching the cylinder, as shown in Figure 14(a). An alternative strategy relies in splitting the computational fluid domain into two sub-domains with independent (non-conforming) meshes, see Figure 14(b): the finer mesh is used to represent the boundary layer around the cylinder while the coarse one for the far field. In the latter case, after space and time discretization of the Navier-Stokes equations, the algebraic form of the linear system to be solved assumes the form of Eq. (21) (in which the matrices $A_{i,j}$ and the right hand sides $\mathbf{f}_i$ are those associated with the fully-discretized Navier-Stokes equations).

The values of the physical parameters for the fluid as well as the boundary conditions used in our simulations are those described in [20]. The essential boundary condition on the fluid velocity at the cylinder surface is imposed in weak form [1, 12].

In Table 10 we report the drag and lift coefficients of the cylinder obtained using different fluid meshes in which the boundary layer refinement was obtained like in Figure 14(a). In Table 11 we report the number of degrees of freedom used when two non-conforming fluid meshes are used: a coarser mesh is used to represent the far field while a finer one around the cylinder. In this example, the mesh-size used for the coarser mesh is the one of Mesh Level 1 while the one of the finer mesh coincides with the mesh-size of Mesh level 4 (see Table 10). Furthermore, the far field domain is considered as slave domain while the one around the cylinder is the master. In this way the interface degrees of freedom of the master (finer) domain are

29
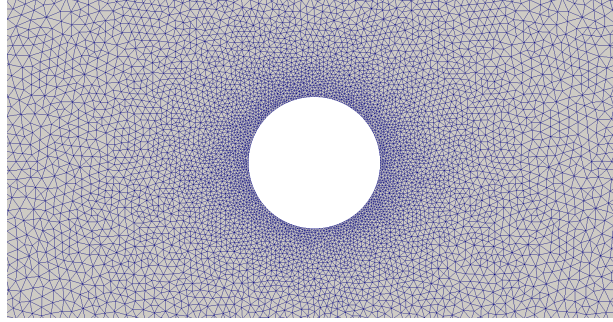
(a) Boundary layer refinement obtained by progressive reduction of the mesh size.
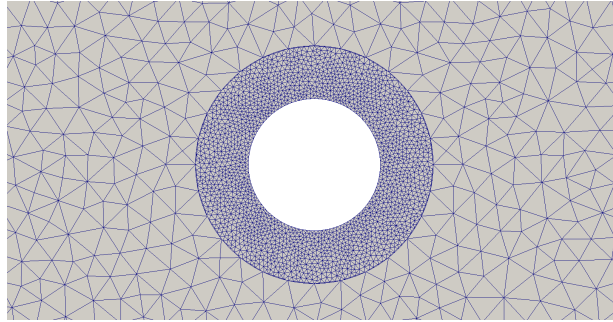
(b) Independent meshes for the far field and the boundary layer zones.

Figure 14: Two different strategies to realize boundary layers mesh refinements.

Mesh level	DOF	C_D	C_L	% error C_D	% error C_L
1	149'004	6.39269	0.003331	3.35	64.56
2	250'400	6.26037	0.005431	1.21	42.22
3	531'992	6.20392	0.006838	0.31	27.26
4	1'209'060	6.17584	0.009412	0.15	0.11

Table 10: Numerical results obtained for the benchmark problem at $Re = 20$. The reference drag and lift coefficients are $C_D = 6.18533$ and $C_L = 0.009401$, respectively.

Domain	Degrees of Freedom
Master	373'068
Slave	103'768

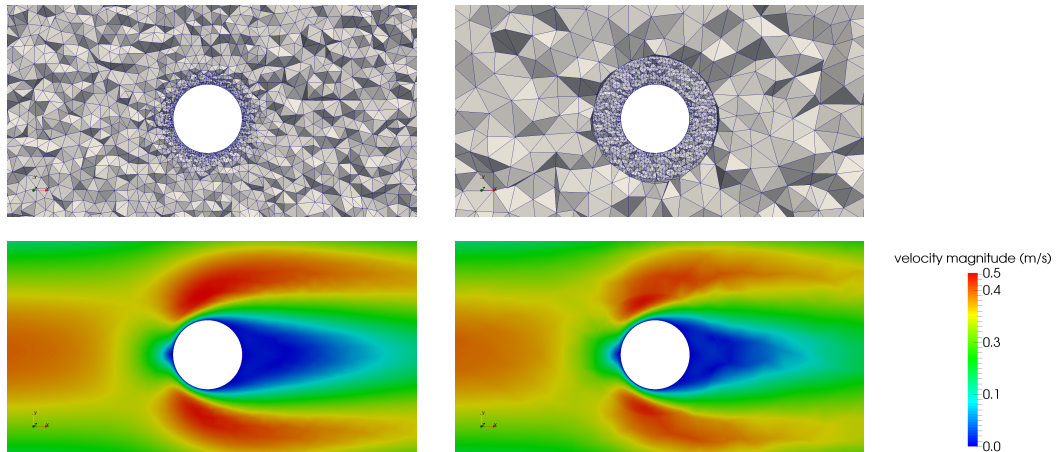Table 11: Number of degrees of freedom for the master and the slave domains.

Figure 15: Zoom of the meshes and the velocity fields in the region close to the cylinder on a cut plane at $z = 0.205\,m$: in the first row we show the meshes used for the numerical simulations. In the second row we plot the velocity fields obtained.

primal unknowns of the problem (see Eq. (21)). We remark that the ratio between the mesh size of the far field and the one in the boundary layer is approximately 6.

The numerical simulation performed using two non-conforming meshes yields a lift coefficient $C_L = 0.009487$ and a drag coefficient $C_D = 6.19713$. The errors with respect to reference values are 0.91% and 0.19% on the estimation of the lift and the drag coefficients, respectively. To analyze the computational costs, we compare the average time to complete a single time step and the number of linear solver iterations on the simulations with Mesh level 4 of Table 10 and the one by INTERNODES with non-conforming meshes. The approach based on the use of non-conforming meshes leads to a reduction of the 50% of the time to perform a time step (mainly due to the fact that the number of degrees with non-conforming meshes is roughly half of the one of Mesh level 4). Furthermore, we observe that the number of linear solver iterations is about 25 in both cases.

Finally, we report the results obtained for $Re = 100$. In Figure 16 we show the fluid meshes considered for the region close to the obstacle and the far field. In this unsteady case, the geometry in which we use a finer mesh is extended to embed also the wake region behind the cylinder. We consider the far field domain as the slave domain, while the one near the cylinder as master. The computational meshes yield 281'393 degrees of freedom in the
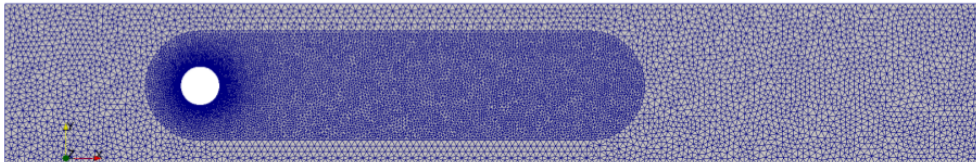
31

Figure 16: Horizontal view of the meshes used for the numerical example at Reynolds 100.

slave domain while 844'179 in the master. We remark that the aspect ratio between the mesh sizes of the master and slave domains at their interface is approximately 3.

In Figure 17 we show the numerical results computed at different times on a cut plane parallel to the z axis (located at at $z = 0.205\,m$): we notice that both the velocity and pressure solutions obtained in the master and slave domains are in very good agreement at their interface. To better assess the behavior of the solution across the interface, in Figure 18 we plot the fluid velocity along a vertical line passing through both the master and slave sub-domains.

Finally, in Table 12, we compare the aerodynamic coefficients of the cylinder computed numerically with those available in literature:

	Maximum C_D	Maximum C_L	Minimum C_L
Computed	3.3017	0.0029	-0.011017
Reference	3.2978	0.0028	-0.010999

Table 12: Comparison of the aerodynamic coefficients computed with reference values available in literature [20].

10. Conclusions

In this work we proposed INTERNODES, an accurate and easy to implement interpolation based method for coupling the solutions of PDEs on subdomains that feature non-conforming discretizations. We considered each individual subdomain discretized by either the finite element or the spectral element method.

The non-conforming problem was formulated in variational form as a generalized Galerkin problem in which the intergrid operator for the data transfer across the non-conforming subdomain interfaces is based on interpolation. The Lagrange and RL-RBF interpolants were considered in this
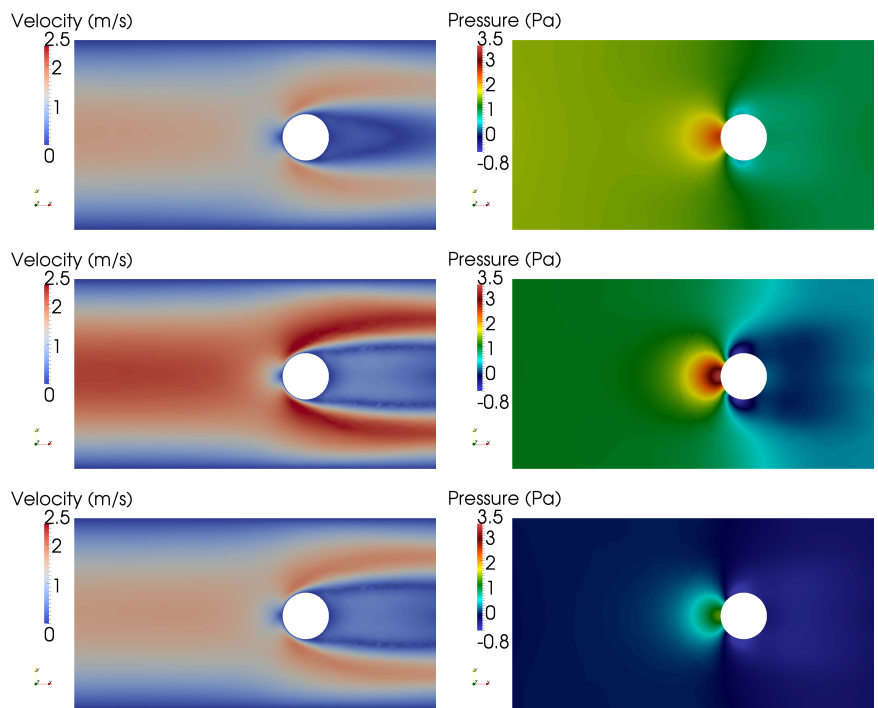
Figure 17: Visualization of the numerical solution obtained at times $t = 2\,s$ (top row), $t = 4\,s$ (middle row) and $t = 6\,s$ (bottom row). On the left column we report the fluid velocity while on the right the fluid pressure.
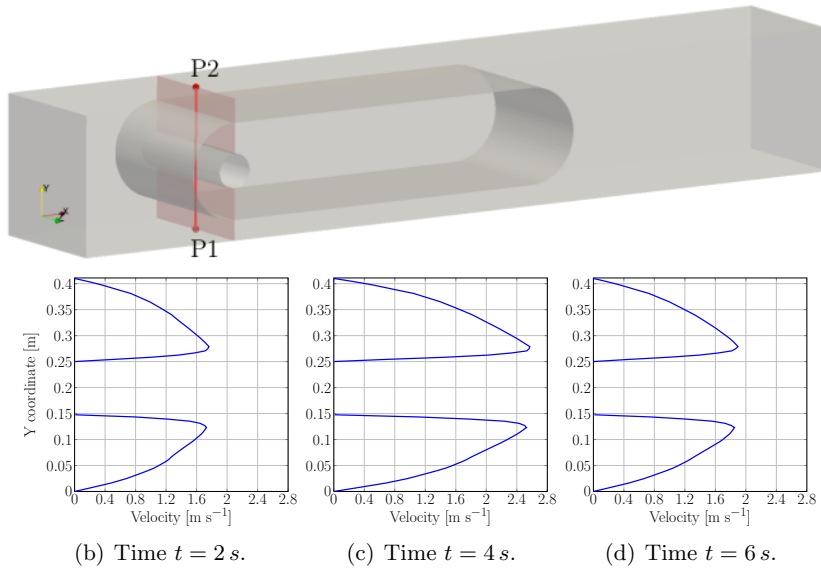
Figure 18: Plot over line, between points P1 = (0.5,0,0.205) and P2 = (0.5,0.41,0.205), of the flow velocity at different times.

work.

We extensively investigated the convergence properties of INTERNODES by solving numerically an elliptic problem in which the subdomains were discretized by non-conforming FEM-FEM, SEM-SEM and SEM-FEM (even in the presence of geometrically non-matching interfaces).

A comparative study with the mortar method was carried out and we showed that the orders of convergence obtained by INTERNODES compare successfully with those generated by mortar.

Finally, we tested the method proposed by solving the benchmark problem of the fluid flow past a cylinder at different Reynolds numbers in which independent (non-conforming) meshes for the boundary layer and the far field parts of the domain were considered.

11. Acknowledgements

References

[1] Y. Bazilevs and T.J.R. Hughes. Weak imposition of dirichlet boundary conditions in fluid mechanics. *Comput. Fluids*, 36:12–26, 2007.

[2] F. Ben Belgacem. The mortar finite element method with Lagrange multipliers. *Numer. Math.*, 84(2):173–197, 1999.

[3] C. Bernardi, Y. Maday, and A.T. Patera. Domain decomposition by the mortar element method. In *Asymptotic and numerical methods for partial differential equations with critical parameters (Beaune, 1992)*, volume 384 of *NATO Adv. Sci. Inst. Ser. C Math. Phys. Sci.*, pages 269–286. Kluwer Acad. Publ., Dordrecht, 1993.

[4] C. Bernardi, Y. Maday, and A.T. Patera. A new nonconforming approach to domain decomposition: the mortar element method. In *Nonlinear partial differential equations and their applications. Collège de France Seminar, Vol. XI (Paris, 1989–1991)*, volume 299 of *Pitman Res. Notes Math. Ser.*, pages 13–51. Longman Sci. Tech., Harlow, 1994.

[5] C. Canuto, M. Y. Hussaini, A. Quarteroni, and T. A. Zang. *Spectral Methods. Evolution to Complex Geometries and Applications to Fluid Dynamics.* Springer, Heidelberg, 2007.

[6] J. A. Cottrell, T. J. R. Hughes, and Y. Bazilevs. *Isogeometric Analysis. Towards Integration of CAD and FEA.* Wiley, Chichester, 2009.

[7] S. Deparis, D. Forti, and A. Quarteroni. A Rescaled Localized Radial Basis Function Interpolation on Non-Cartesian and Nonconforming Grids. *SIAM J. Sci. Comp.*, 36:A2745–A2762, 2014.

[8] T. Dickopf and R. Krause. Efficient simulation of multi-body contact problems on complex geometries: A flexible decomposition approach using constrained minimization. *Int. J. Numer. Meth. Engng*, 77:1834–1862, 2009.

[9] L. Formaggia, A. Quarteroni, and A. Veneziani, editors. *Cardiovascular mathematics*, volume 1 of *MS&A. Modeling, Simulation and Applications.* Springer-Verlag Italia, Milan, 2009. Modeling and simulation of the circulatory system.

[10] D. Forti and L. Dedè. Semi–implicit BDF time discretization of the Navier–Stokes equations with VMS–LES modeling in High Performance Computing framework. *Comput. Fluids*, 117:168–182, 2015.

[11] P. Gervasio, F. Saleri, and A. Veneziani. Algebraic fractional step schemes with spectral methods for the incompressible Navier-Stokes equations. *J. Comput. Phys.*, 214(1):347–365, 2006.

[12] M.C. Hsu, I. Akkerman, and Y. Bazilevs. Wind turbine aerodynamics using ale–vms: validation and the role of weakly enforced boundary conditions. *Comput. Mech.*, 50:499–511, 2012.

[13] T. Klöppel, A. Popp, U. Küttler, and W.A. Wall. Fluid-structure interaction for non-conforming interfaces based on a dual mortar formulation. *Comput. Methods Appl. Mech. Engrg.*, 200:3111–3126, 2011.

[14] M. Lombardi, N. Parolini, A. Quarteroni, and G. Rozza. Numerical simulation of sailing boats: Dynamics, fsi, and shape optimization. In G. Buttazzo and A. Frediani, editors, *Variational Analysis and Aerospace Engineering: Mathematical Challenges for Aerospace Design*, pages 339–377. Springer, 2012.

[15] N. Parolini and A. Quarteroni. Mathematical models and numerical simulations for the americas cup. *Comput. Methods Appl. Mech. Engrg.*, 194(9):1001–1026, 2005.

[16] A. Quarteroni. *Numerical Models for Differential Problems.* 2nd edition. Series MS&A, Vol. 2. Springer, Milano, 2013.

[17] A. Quarteroni and A. Valli. *Numerical Approximation of Partial Differential Equations.* Springer Verlag, Heidelberg, 1994.

[18] A. Quarteroni and A. Valli. *Domain Decomposition Methods for Partial Differential Equations.* Oxford Science Publications, 1999.

[19] P. Reymond, P. Crosetto, S. Deparis, A. Quarteroni, and N. Stergiopulos. Physiological simulation of blood flow in the aorta: comparison of hemodynamic indices as predicted by 3-d fsi, 3-d rigid wall and 1-d models. *Medical engineering & physics*, 35(6):784–791, 2013.

[20] M. Schäfer and S.Turek. Benchmark computations of laminar flow around a cylinder. In E. Hirschel, editor, *Flow Simulation with High-Performance Computers II. DFG priority research program results*

1993-1995, number 52 in Notes Numer. Fluid Mech., pages 547–566. Vieweg, Weisbaden, 1996.

[21] S.J. Sherwin and G.E. Karniadakis. A triangular spectral element method; applications to the incompressible Navier-Stokes equations. *Comp. Meth. Appl. Mech. Engrg.*, 123:189–229, 1995.

[22] B. I. Wohlmuth. A mortar finite element method using dual spaces for the Lagrange multiplier. *SIAM J. Numer. Anal.*, 38:989–1012, 2000.

MOX Technical Reports, last issues

Dipartimento di Matematica
Politecnico di Milano, Via Bonardi 9 - 20133 Milano (Italy)

42/2015 Brugiapaglia, S.; Nobile, F.; Micheletti, S.; Perotto, S.
A theoretical study of COmpRessed SolvING for advection-diffusion-reaction problems

41/2015 Quarteroni, A.; Veneziani, A.; Vergara, C.
Geometric multiscale modeling of the cardiovascular system, between theory and practice

40/2015 Patelli, A.S.; Dedè, L.; Lassila, T.; Bartezzaghi, A.; Quarteroni, A.
Isogeometric approximation of cardiac electrophysiology models on surfaces: an accuracy study with application to the human left atrium

39/2015 Guglielmi, A.; Ieva, F.; Paganoni, A.M.; Quintana, F.A.
A semiparametric Bayesian joint model for multiple mixed-type outcomes: an Application to Acute Myocardial Infarction

38/2015 Grasso, M.; Menafoglio, A.; Colosimo, B.M.; Secchi, P.
Using Curve Registration Information for Profile Monitoring

36/2015 Fedele, M.; Faggiano, E.; Barbarotta, L.; Cremonesi, F.; Formaggia, L.; Perotto, S.
Semi-Automatic Three-Dimensional Vessel Segmentation Using a Connected Component Localization of the Region-Scalable Fitting Energy

37/2015 Aletti, M.; Perotto, S.; Veneziani, A.
Educated bases for the HiMod reduction of advection-diffusion-reaction problems with general boundary conditions

32/2015 Agasisti,T.; Ieva, F.; Masci, C.;Paganoni, A.M.
Does class matter more than school? Evidence from a multilevel statistical analysis on Italian junior secondary school students

34/2015 Bernardi, M.S.; Mazza, G.; Ramsay, J.O.; Sangalli, L.M.
A separable model for spatial functional data with application to the analysis of the production of waste in Venice province

33/2015 Fumagalli, A; Pasquale, L; Zonca, S.; Micheletti, S.
An upscaling procedure for fractured reservoirs with non-matching grids